arXiv:1606.08700v1 [astro-ph.HE] 28 Jun 2016

First detection at 5.5 and 9 GHz of the radio relics in bullet cluster with ATCA

Siddharth Malu[1], Abhirup Datta[1,2] and Pritpal Sandhu[1]

ABSTRACT

We present here results from observations at 5.5 and 9 GHz of the Bullet cluster 1E 0657−55.8 with the Australia Telescope Compact Array (ATCA). Our results show detection of diffuse emission in the cluster. Our findings are consistent with the previous observations by Shimwell *et al.* (2014) & Shimwell *et al.* (2015) at 1.1–3.1 GHz. Morphology of diffuse structures (relic regions A and B and the radio halo) are consistent with those reported by the previous study. Our results indicate steepening in the spectral index at higher frequencies ($\gtrsim$ 5.0 GHz) for region A. The spectrum can be fit well by a broken power law. We discuss the possibility of a few recent theoretical models explaining this break in the power law spectrum, and find that a modified Diffusive Shock Acceleration (DSA) model or a turbulent reacceleration model may be relevant. Deep radio observations at high frequencies ($\gtrsim$ 5 GHz) are required for a detailed comparison with this model.

Subject headings: cosmic microwave background — galaxies: clusters: individual (1E 0657–56, RX J0658–5557) — intergalactic medium — radio continuum: general — techniques: interferometric

1. Introduction

Galaxy clusters have been studied extensively in X-rays (Sarazin 1988) and radio (Brunetti and Jones 2014; Feretti *et al.* 2012). Galaxy clusters grow by mergers with other clusters and galaxy groups. These mergers create shock waves within the ICM that can accelerate particles to extreme energies, with the compression of magnetic fields along shock fronts causing an additional systematic pressure enhancement. These shocks can be studied through two different processes – Brehmsstrahlung (through X-ray observations) and Synchrotron (through radio), and they probe thermal and non–thermal populations of electrons.

Diffuse non-thermal radio emission in clusters of galaxies of ∼Mpc size not associated with galaxies, when close to the centres of clusters, are called *radio halos*, and when at or close to the

[1]Centre of Astronomy, Indian Institute of Technology Indore, Simrol, Khandwa Road, Indore 452020, India

[2]Center for Astrophysics and Space Astronomy, Department of Astrophysical and Planetary Science, University of Colorado, Boulder, C0 80309, USA

peripheries of clusters are called *radio relics*. These are associated with relativistic electrons and magnetic fields in the ICM.

1E0657−56, known as the 'Bullet Cluster', is one of the hottest known clusters (with X-ray luminosity L_X $\sim$4.3$\times10^{45}$ ergs s^{-1}; temperature $kT \sim$ 14.7 keV) that has been well-studied over the last decade for a variety of reasons; namely, the existence of a cold front in the X–ray observations (Owers *et al.* 2009) a strong radio halo (Liang *et al.* 2000), the Sunyaev-Zel'dovich effect (Halverson *et al.* (2009), Plagge *et al.* (2010) and references therein), though most notably in providing the most direct proof of the existence of dark matter (Clowe *et al.* 2006). It is a cluster collision/merger event at z $\sim$0.296, with the larger, eastward cluster being $\sim$10 times the mass of the smaller 'bullet'.

A powerful radio halo in the Bullet cluster was first reported by Liang *et al.* (2000), who detected the radio halo using the ATCA as well as 843 MHz Molonglo Observatory Synthesis Telescope (MOST). Analysis of data in Liang *et al.* (2000) centered on a 3.5 Mpc^2 region defined by them on the basis of the extent of diffuse emission observed at 1.3 GHz.

Shimwell *et al.* (2014) reported deep observations of the cluster at 2.1 GHz, with a noise rms of 15μJy beam^{-1}, a significant improvement over Liang *et al.* (2000). This was made possible by two upgrades of the Australia Telescope Compact Array (ATCA) – addition of a N–S spur, and the increase in bandwidth by a factor of 16, through the Compact Array Broadband Backend, or CABB (Wilson *et al.* 2011). These two upgrades improved the sensitivity of ATCA by a factor of $\sim$4, and enabled deep observations of Bullet cluster at 2.1 GHz and higher frequencies.

Shimwell *et al.* (2014) constructed a spectral index map of the Bullet cluster, and detected polarization in a certain region. Shimwell *et al.* (2015) studied this region in more detail, and confirmed that it has the characteristics of a relic. They then proceeded to estimate the total brightness of the two components marked 'Region A' & 'Region B' in four sub–bands, and derive spectral indices -1.07 ± 0.03 and -1.66 ± 0.14 for the two components respectively. They also interpret 'Region B' as a second shock front. One of the most important aspects of the detection and characterization of diffuse emission in Shimwell *et al.* (2014) and Shimwell *et al.* (2015) is their "in–band" spectral index estimation, i.e. determination of spectral index within the 1.1–3.1 GHz ATCA band.

2.1 GHz deep observations of Shimwell *et al.* (2014) and Shimwell *et al.* (2015) are critical not only for an accurate estimation of the radio halo / relic flux, but also to accurately determine the spectral index of both the radio halo and the radio relic. As a practical matter, it is in fact easier to estimate the total flux and spectral index of the radio relic as compared to the radio halo, since halos, due to their central location in cluster mergers, are likely to be in the vicinity of several point sources (bright radio galaxies).

We summarize our observations in §2, describe data reduction in §3, present results in §4 (5.5 GHz results in §4.1, 9 GHz results in §4.2 and the radio relics in §4.3), and discuss the results in §5.

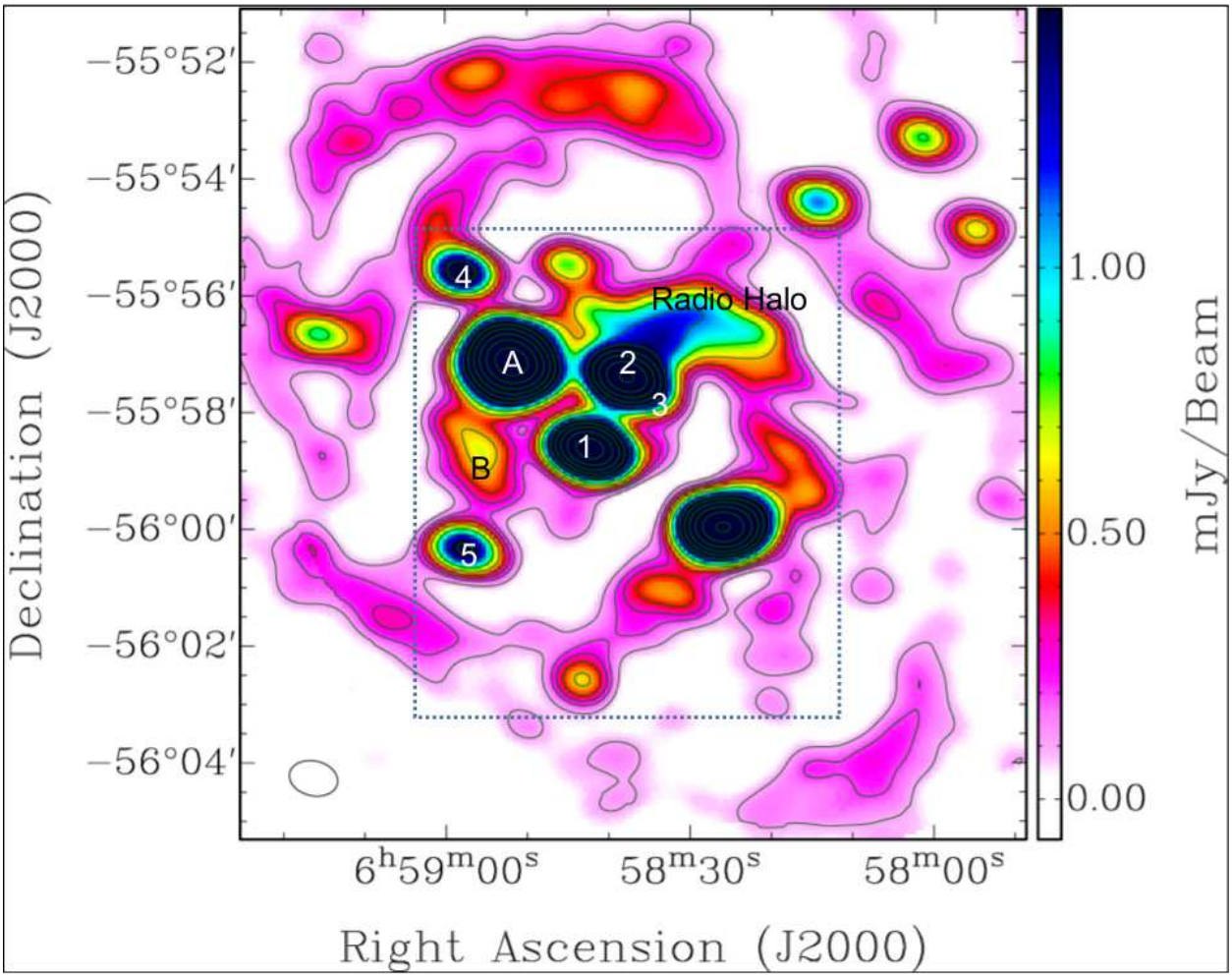

Fig. 1.— 5.5 GHz radio image of the Bullet cluster, observed with H168 array of the ATCA, with a synthesized beam $50.5'' \times 35.9''$ (indicated as an ellipse in the bottom left corner). This is a natural–weighted image, and the extent of this image is similar to the figures in Shimwell *et al.* (2014). Noise rms ($\sigma_{\rm RMS}$) is 20μJy/beam. Contour levels are at $-5, 5, 10, 15, 20, 40, 80, 160, 320, 640 \times \sigma$.

2. Observations

The Australia Telescope Compact Array (ATCA) is a radio interferometer with six 22m antennas, five of which may be positioned on stations along a T-shaped rail track that is 3-km along E-W and 214-m along N-S.

The bullet cluster was observed for a total duration of 14 hours in the 6 cm and 3 cm bands with centre frequencies 5.5 GHz and 9 GHz respectively, in a 2–pointing mosaic, with the pointing centers at (J2000 epoch coordinates) RA: $06^{\rm h}58^{\rm m}30^{\rm s}$, DEC: $-55°57'00''$ and RA: $06^{\rm h}58^{\rm m}20^{\rm s}$, DEC: $-55°56'00''$ respectively. Table 1 lists the total amount of time spent on these two pointings, and

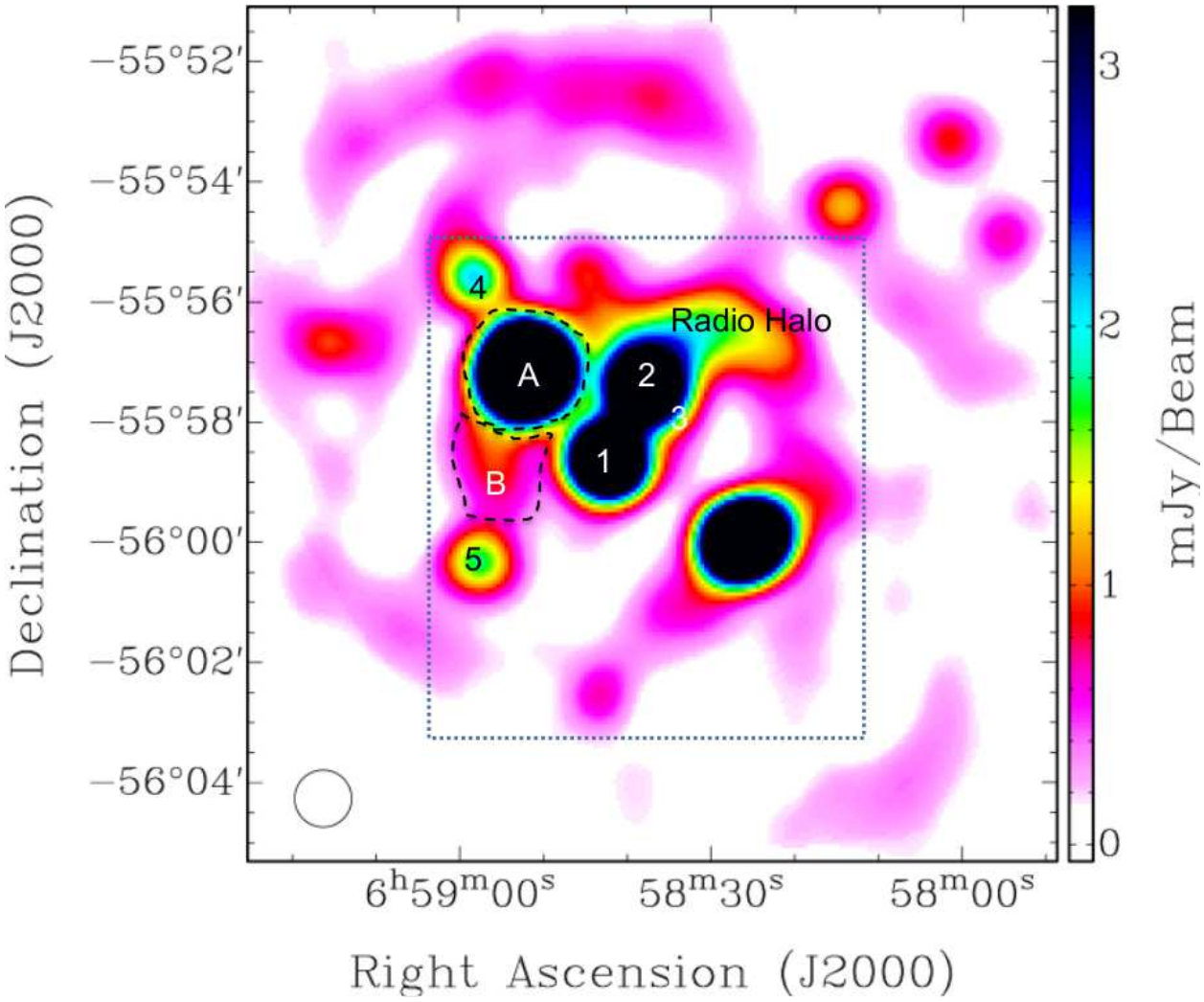

Fig. 2.— 5.5 GHz radio image of the Bullet cluster, observed with H168 array of the ATCA, with a synthesized beam $57'' \times 57''$ (indicated as an ellipse in the bottom left corner). This is a natural–weighted image, and the extent of this image is similar to the figures in Shimwell *et al.* (2014). Noise rms ($\sigma_{\rm RMS}$) is 20μJy/beam. Regions A & B, and the six point sources are marked in the figure. Properties of the point sources and regions A & B are given in Tables 2 and 3. The dashed box indicates the area in the image that we have described in this paper. The two dashed areas indicate roughly the extents of the regions A and B.

in slewing and calibration. Imaging from visibilities in this mosaic is described in §3.

Observations were made in the H168 array that has a maximum baseline up to 192-m (using

the five antennas in the array) and a minimum baseline of 61-m. A summary of the observations is in Table 1. Observations of the Bullet cluster were made in a pair of 2-GHz bands: a '5.5-GHz band' covering frequencies 4.5–6.5 GHz and a '9-GHz band' covering the range 8–10 GHz. Each of the 2-GHz wide bands were subdivided into 2048 frequency channels. All observations were in full polarization mode and recorded multi-channel continuum visibilities. In each observing session, antenna pointing corrections were updated every hour using a 5–point offset pattern observation on a bright calibrator, unresolved phase calibrators were observed every 60 min to monitor and correct for amplitude and phase drifts in the interferometer arms, and PKS B1934–638 was observed once every session as a primary calibrator to set the absolute flux density scale. Visibilities were recorded with 10 sec averaging.

PKS B1934−638 was used as the primary calibrator, and PKS B0823−500 was used as a phase & bandpass calibrator.

The synthesized beam is much larger than in Shimwell *et al.* (2014) because of our observations being made in the second–most compact configuration at the ATCA, namely, H168. This restricts the longest baseline to 168-m, or $\sim$3kλ.

The Compact Array Broadband Backend, described in Wilson *et al.* (2011), was used, with two independent 2048 MHz windows (dual polarization) for correlation, with 1 MHz resolution, which is the standard setting for continuum observations.

3. Data Reduction

Data were analysed using the Multichannel Image Reconstruction, Image Analysis and Display (MIRIAD, developed by ATNF-CSIRO); all image processing were also accomplished using utilities in this software package.

Adopted fluxes for the primary calibrator PKS B1934−638 were 4.965 and 2.700 Jy in the 6-cm and 3-cm bands respectively; the spectral index was adopted to be −1.23 in both bands (see Sault (2003)). Outliers in the amplitudes of visibility data on PKS B1934−638 were rejected—removing $\sim$10% of data—and the reliable visibilities were used to set the absolute flux density scale as well as determine the instrument bandpass calibration.

Table 1: Summary of the ATCA observations

Array	Frequency (GHz)	Observing time (hours)	Date
H168	5.5	10.0	2010 July 30
H168	5.5	4.0	2010 July 31
H168	9.0	10.0	2010 July 30
H168	9.0	4.0	2010 July 31

When calibrated for the bandpass, the visibility amplitudes of PKS B0823−500 showed continuity across both the 2-GHz observing frequency ranges and a trend consistent with a single power-law: this was a check of the bandpass calibration. Drifts of up to 30° were observed in the interferometer arms over the observing sessions: calibrations for the time-varying complex gains in the antenna signal paths as well as calibrations for polarization leakages were derived from the visibilities on PKS B0823−500. RMS phase variations in antenna signal paths within the 1-min calibrator scans was within 0.5°, indicating that short timescale atmospheric and instrumental phase cycling would result in amplitude attenuation of less than 1%.

The visibility data in the 5.5 and 9 GHz bands were separately edited for interference and calibrated before bandwidth synthesis imaging. Visibility data in each of the 2 GHz wide bands were recorded over 2048 frequency channels, and 50 channels at each of the band edges were excluded from analysis to avoid data in frequency domains where signal path gains are relatively low. Frequency channels that appeared to have relatively large fluctuations in visibility amplitude owing to hardware faults in the digital correlator were also rejected prior to calibration and imaging.

Since no circular polarization is expected, Stokes V is expected to be consistent with thermal noise, and we make estimates of noise rms from Stokes V, following Subrahmanyan *et al.* (2000). Therefore, at times and frequency channels where Stokes V visibilities deviate more than four times rms thermal noise in the calibrated visibilities acquired towards the cluster pointings, data in all Stokes parameters were rejected. Stokes–V based clipping was therefore done, aimed at automated rejection of self-generated low level interference. In order to carry out Stokes–V based clipping, the Miriad task Tvclip was used to find the median and rms levels for every channel, and then all visibilities beyond the median $\pm 5\sigma$ were flagged, and the same flagging was applied to all the other Stokes parameters. This procedure was then repeated for every Stokes parameter. This way, 25% of the data at 5.5 GHz and 20% of the data at 9 GHz were flagged.

We note here that our observations were made in 2010, when the CABB system (Wilson *et al.* 2011) was relatively new, and therefore, noise per channel was higher, resulting in a higher T_{sys}, i.e. system temperature/lower sensitivity than is currently possible. Going through our raw ATCA data, we find that the typical T_{sys} in our data is $\sim$ 80–100K, whereas current estimates of T_{sys} are in the range 40–50 K.

In order to mosaic the two pointings, we follow the scheme provided by Sault *et al.* (1996); namely, make a mosaic of all the data, leading to a mosaicked dirty image, using the option 'mosaic' in the Miriad task Invert. Then, deconvolution was done using Miriad task Mossdi, which allows a joint deconvolution of mosaicked images.

Table 2: Unresolved and diffuse continuum radio sources detected in the Bullet cluster field

Source Label	RA (J2000)			DEC (J2000)			Diffuse or point source	Int. Flux Density $S_{5.5\ \mathrm{GHz}}$	Int. Flux Density $S_{9\ \mathrm{GHz}}$	Shimwell *et al.* (2014) Label
	h	m	s	°	′	″		(mJy)	(mJy)	
Region A	06	58	51.91	−55	57	07.9	Diffuse	18.04 ± 0.40	4.36±0.15	Region A
Region B	06	58	55.26	−55	58	47.8	Diffuse	0.88 ± 0.08	0.09±0.02	Region B
1	06	58	42.3	−55	58	37.5	Point	8.69 ± 0.20	2.65 ± 0.11	M
2	06	58	37.6	−55	57	24.0	Point	7.54 ± 0.18	4.36 ± 0.13	L
3	06	58	34.3	−55	57	40.0	Point	0.60 ± 0.10	Detected	K
4	06	58	58.1	−55	55	35.1	Point	2.16 ± 0.02	0.43 ± 0.02	Detected
5	06	58	57.8	−56	00	20.1	Point	1.89 ± 0.02	0.39 ± 0.04	Detected
6	06	58	14.6	−55	54	23.0	Point	0.99 ± 0.01	0.75± 0.04	N

NOTES– Letters indicate diffuse sources; numbers indicate discrete (point) sources from our 5.5 & 9 GHz observations. Regions of diffuse emission are marked with letters on Fig. 2 and Fig. 4.

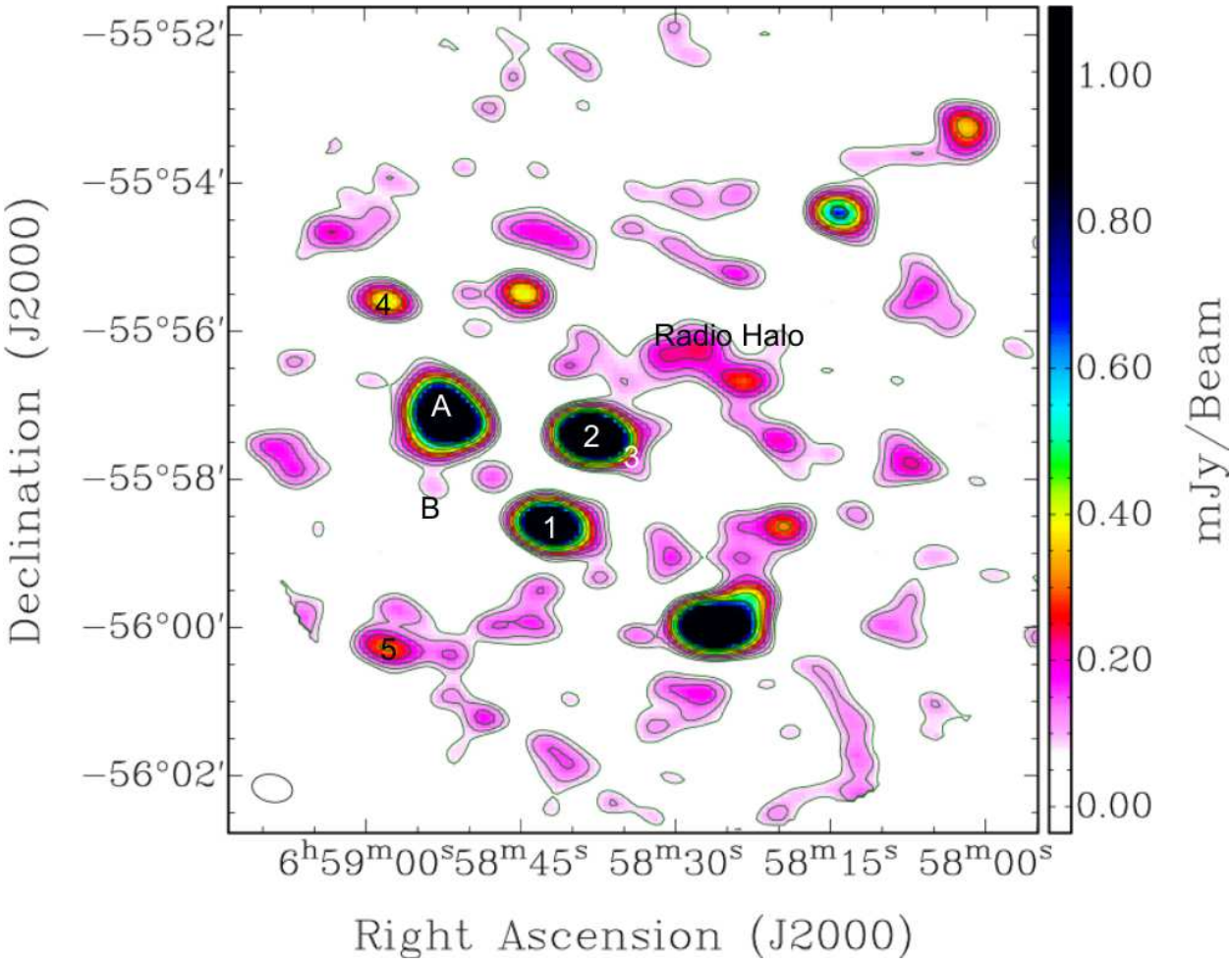

Fig. 3.— 9 GHz radio image of the Bullet cluster, observed with H168 array of the ATCA, with a synthesized beam $33.1'' \times 22.3''$ (indicated as an ellipse in the bottom left corner). This is a natural–weighted image, and the extent of this image is similar to the figures in Shimwell *et al.* (2014). Noise rms ($\sigma_{\rm RMS}$) is 15μJy/beam. Contour levels are at $-5, 3, 5, 7.1, 10, 14, 20, 28, 40 \times \sigma$. Regions A & B, and the six point sources are marked in the figure.

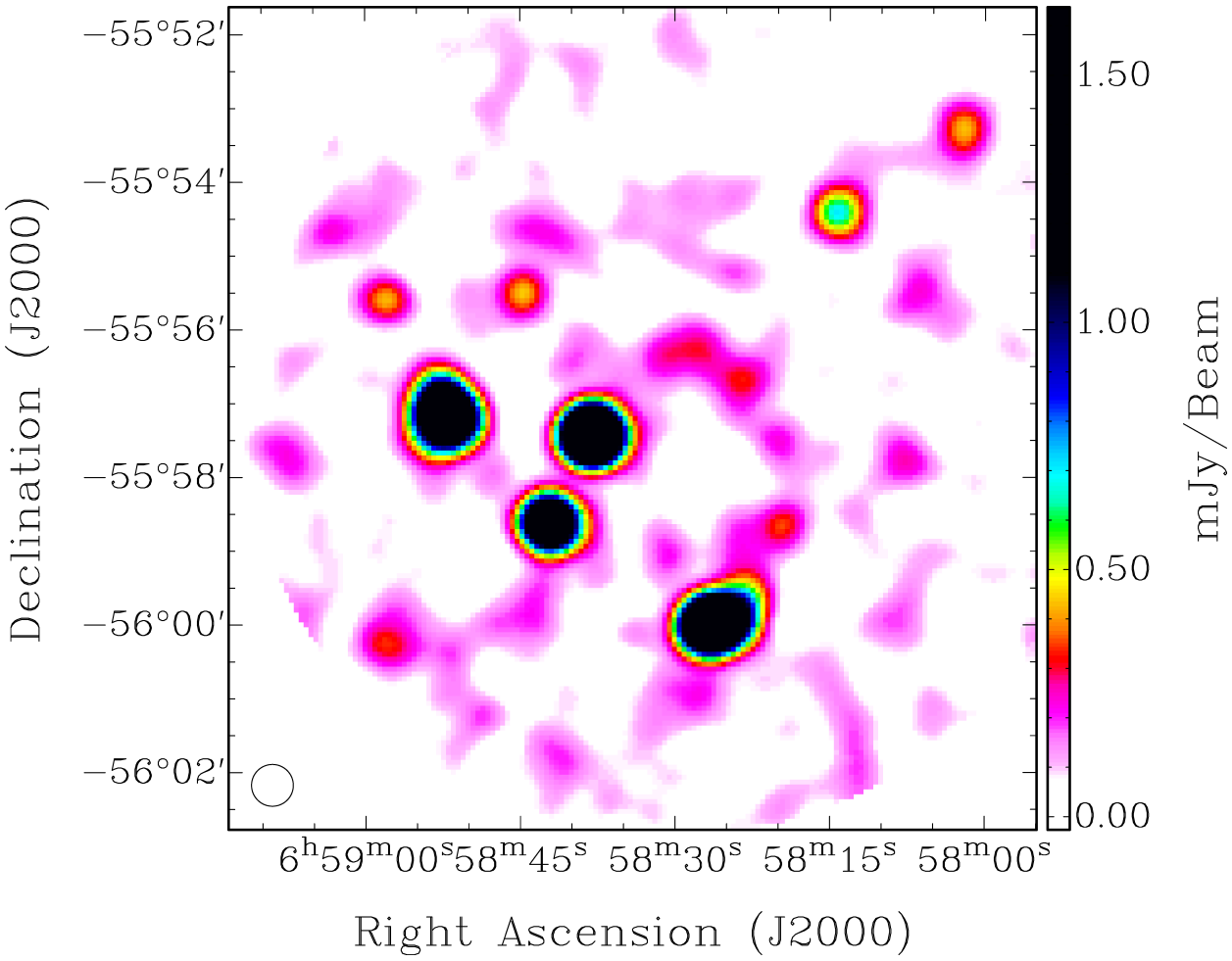

Fig. 4.— 9 GHz radio image of the Bullet cluster, observed with H168 array of the ATCA, with a synthesized beam $34'' \times 34''$ (indicated as an ellipse in the bottom left corner). This is a uniform–weighted image, and the extent of this image is similar to the figures in Shimwell *et al.* (2014). Noise rms ($\sigma_{\rm RMS}$) is 25μJy/beam.

4. Results – continuum imaging

4.1. Radio Image at 5.5 GHz

Following the analysis described in previous sections, we obtained a radio image of the bullet cluster field, which is shown in Fig. 1. This image was made with natural weighting, and so were all the subsequent images. It should be noted that the intrinsic resolution of this image is $50.5'' \times 35.9''$. A list of point sources, and of regions with diffuse emission, with their location and total emission, is given in Table 2; locations of all point sources match with the values in Shimwell *et al.* (2014).

There is clear evidence of diffuse emission at 5.5 GHz, which occurs in the same region as the 2.1 GHz image (Fig. 5) in Shimwell *et al.* (2014). To facilitate comparison with the 2.1 GHz observations in Shimwell *et al.* (2014), another figure has been made with a synthesized beam of $57'' \times 57''$. Most baselines in the Shimwell *et al.* (2014) 2.1 GHz image are $\gg 5\mathrm{k}\lambda$, so it is not surprising that the diffuse emission we find in the 5.5 GHz image is similar as compared to 2.1 GHz (Shimwell *et al.* 2014) – morphologically. The total amount of diffuse emission in these regions is stated in Table 2.

There is clear detection of the radio halo and two components of the radio relic, as described in Shimwell *et al.* (2014) and Shimwell *et al.* (2015) – these are clearly marked in Fig. 2.

Qualitatively, diffuse emission in Fig. 2 is in good agreement with the 2.1 GHz image (Fig. 5) in Shimwell *et al.* (2014) – both in terms of extent and morphology. In particular, the radio halo at 5.5 GHz has a similar morphology and extent as the halo at 2.1 GHz in Shimwell *et al.* (2014). We also detect – at relatively low significance – a bridge between the radio halo and Region A. Like Shimwell *et al.* (2014), we detect more than one local maxima in the radio halo, and two of these local maxima coincide with the X–ray brightness centers, as in the 2.1 GHz image. The radio halo is extended along the merger axis, the physical extent of the radio halo is more along the merger axis than perpendicular to it, and there is a well–defined western edge, again, like the 2.1 GHz image in Shimwell *et al.* (2014).

4.2. Radio Image at 9 GHz

A low–resolution natural–weighted image at 9 GHz of the Bullet cluster, with a synthesized beam of $33.1'' \times 22.3''$ is shown in Fig. 3, and clearly shows diffuse emission is several regions – region A, region B and radio halo. Another image, with synthesized beam $34'' \times 34''$ (Fig. 4) was made to compute the spectral index of regions A & B. Region A is very prominent, but region B is barely detectable, and part of region B are absent, implying that the spectrum might have steepened.

There are several similarities with the 2.1 and 5.5 GHz images; for instance, just as in Shimwell *et al.* (2014) and §4.1, we detect more than one local maxima in the radio halo, and two of these local maxima coincide with the X–ray brightness centers, just as in the 2.1 and 5.5

GHz images – the third local maxima coinciding with the local maxima in radio halo at 5.5 GHz. The radio halo is extended along the merger axis, just as at 2.1 and 5.5 GHz, and there is a well–defined western edge, just as in the 2.1 and 5.5 GHz images. In other words, features of the radio halo at 9 GHz match qualitatively with the features detected by Shimwell *et al.* (2014).

4.3. Radio relic at 5.5 and 9 GHz

Shimwell *et al.* (2015) have detected and characterized relics in the Bullet cluster at 2.1 GHz. They measured the brightness, substructure and polarization properties of the two relic regions. They interpret Region B as a second shock front, and also comment on the high brightness of Region A, and speculate on its origin.

In this paper, we have detected both relic regions A and B in our 5.5 and 9 GHz observations (Figs. 1, 2, 3 & 4). Peak emission occurs at RA: $06^{\rm h}58^{\rm m}51.91^{\rm s}$, DEC: $-55°57'7.88''$ at 5.5 GHz, and at RA: $06^{\rm h}58^{\rm m}51.91^{\rm s}$, DEC: $-55°57'11.88''$ at 9 GHz, the difference between the two positions being $4''$, which is a fraction of the beamsize. Our definitions of Relic Regions 'A' and 'B' are exactly the same as in Shimwell *et al.* (2015) – with the same extents in declination.

The general large–scale morphology of Regions A and B is roughly similar to figures 1 & 3 in Shimwell *et al.* (2015); however, our observations lack angular resolution, so it is not possible to tell whether the high–resolution structure at 5.5 and 9 GHz is similar to the 2.1 GHz structure.

We have measured the integrated flux of the diffuse radio emission as a function of frequency for regions A and B (see Fig. 5) and characterized the 4.5 to 6.5 GHz & 8 to 10 GHz emission. Following Shimwell *et al.* (2015), we calculated the uncertainty on our integrated flux density measurements by adding in quadrature the ATCA absolute flux calibration error of 2 per cent (Reynolds 1994), with the error on the integrated flux density derived from the image noise. Flux densities for regions A and B at 5.021, 5.468, 5.944 and 9.013 GHz are provided in Table 3.

In computing the spectral index, we have taken also taken into account the flux densities of regions A and B as presented in Fig. 2 in Shimwell *et al.* (2015). Following Fig. 5, we obtain the mean spectral index of region A to be $-1.41^{+0.09}_{-0.07}$ between 1.1 and 9.0 GHz. For region B, we obtain a mean spectral index of $-1.70^{+0.35}_{-0.31}$ between 1.1 and 9.0 GHz. For region A, we have also fit for a

Table 3: Diffuse emission in Relic Regions A & B in C and X bands

Frequency (MHz)	Region A (mJy)	Region B (mJy)
5021	19.05 ± 0.20	0.88 ± 0.08
5468	18.04 ± 0.20	0.78 ± 0.07
5944	12.86 ± 0.13	0.66 ± 0.05
9013	04.36 ± 0.15	0.09 ± 0.02

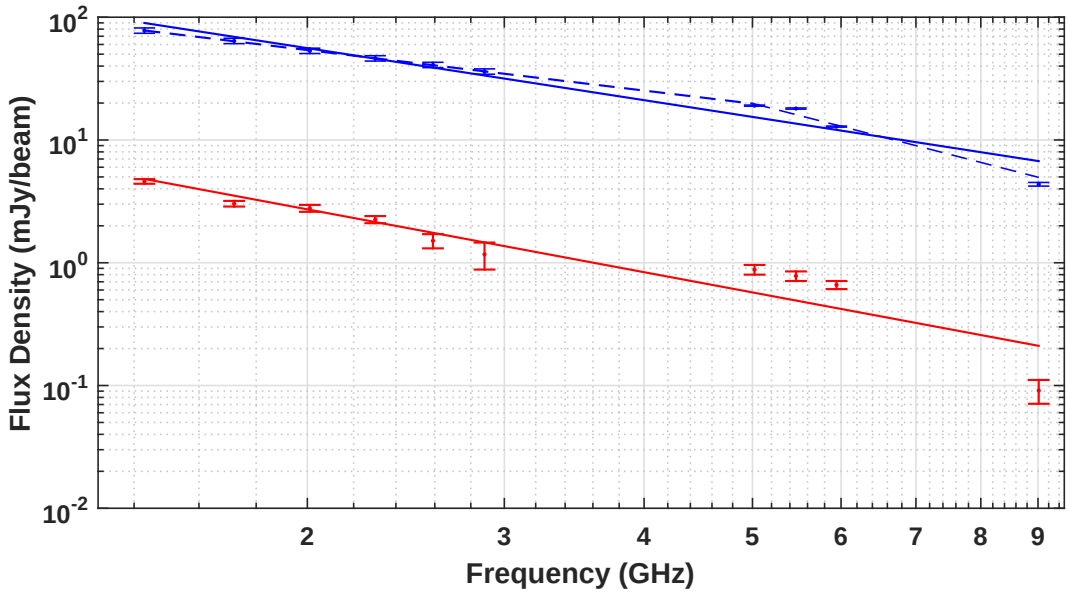

Fig. 5.— Spectral Energy Density of Relic Regions A and B between 1.1 and 9 GHz. Data points for 5.0 and 5.9 GHz are taken from Fig. 2 and data points for 9.0 GHz are taken from Fig. 4. Data points between 1.1 and 3.1 GHz are taken from Fig. 2 of Shimwell *et al.* (2015). Blue represents Region A and red represents Region B. The solid blue line indicates a single spectral index fit for region A, and dashed blue lines represent a 2–index model for region A. See the discussion in §4.3.

2–spectral index model: one between 1.1 and 5.0 GHz and the other between 5.0 and 9.0 GHz. 1.1 to 3.1 GHz data is from Shimwell *et al.* (2014) and Shimwell *et al.* (2015). The two mean spectral indices are $\alpha_{5.0}^{1.1} = -1.1$ and $\alpha_{9.0}^{5.0} = -2.4$. We present the spectrum of Relic Regions A and B in the 1.1–10 GHz range, in Fig. 5.

As can be seen from Fig. 5, the 2-spectral index model fits the data really well, which hints at the existence of a break in the power law between 1 and 9 GHz. A similar steepening was reported in Stroe *et al.* (2014) for the 'Sausage' cluster. It should be noted that such high–frequency steepening is inconsistent with Diffusive Shock Acceleration theory (Drury 1983). Stroe *et al.* (2014) state that high-frequency steepening could be caused by an inhomogeneous medium with temperature/density gradients, or by lower acceleration efficiencies of high-energy electrons. This is discussed in §5.

4.4. A note on the radio halo at 5.5 and 9 GHz

As mentioned in §4.1 and §4.2, the radio halo is easily detectable at both 5.5 and 9 GHz in our observations, and we also detect several peaks in the radio halo, spread along the merger axis of the cluster. Despite this, we have not done a detailed analysis at 5.5 and 9 GHz, because our observations lack the angular resolution to identify and characterize point sources, in order to exclude them from estimates of diffuse emission flux. The only details we provide here are as follows. Integrated flux of the radio halo within the 5σ contours, which is 7.1±0.3 mJy at 5.5 GHz and 1.6±0.3 mJy at 9 GHz. We do not compute the spectral index for the radio halo, since point–sources were not subtracted to get the above estimates. Improved data at 5.5 and 9 GHz with other ATCA configurations are essential for estimating the spectral index of the radio halo. We have applied for more time on the ATCA, with arrays that will provide higher resolution.

4.5. Point sources at 5.5 and 9 GHz

We present detection of 6 point sources in the Bullet cluster field at 5.5 and 9 GHz. Each one of these displays interesting features, especially the possible presence of jets. Sources 1,2,3,6, whose properties are described in Table 2 in Shimwell *et al.* (2014), were also detected by us; their properties are listed in Table 2.

5. Discussion

In this paper, we have presented the first detections of diffuse emission in the Bullet cluster at 5.5 and 9 GHz, using the ATCA (radio halo and relic regions A & B). We summarize the essential results as below:

1. The brightest part of diffuse emission in the cluster is a northern relic (referred to in Shimwell *et al.*

(2015) and in this paper as Region A) – significantly brighter than all other diffuse features, and unusually bright at 5.5 and 9 GHz, like the 2.1 GHz observations

2. There is a second shock front – named Region B – immediately to the south of Region A, which is elongated along N–S

3. At very low resolutions ($57''$ at 5.5 GHz and $34''$ at 9.0 GHz), morphology of regions 'A' and 'B' are similar at 5.5 and 9 GHz compared to 2.1 GHz

4. Morphology and extent of the radio halo in the cluster are similar at 5.5, 9.0 and 2.1 GHz

5. Spectral index calculation shows a steepening at higher frequencies for Region A, which can best be characterized by a broken power law near 5.0 GHz.

Diffuse emission in cluster mergers has been detected at high frequencies (> 5 GHz) for the Bullet and other clusters (Malu *et al.* 2010; Malu and Subrahmanyan 2011); in particular, Stroe *et al.* (2016) have charaterized the spectrum of the 'Sausage' and 'Toothbrush' radio relics (van Weeren *et al.* 2010, 2012) from 150 MHz to 30 GHz. Therefore, a detection of the radio relic in the Bullet cluster at 5.5 and 9 GHz is unsurprising.

While an ideal Diffusive Shock Acceleration (DSA) model (e.g. Drury (1983)) does not predict a break in the spectrum, more realistic models predict a gradual steepening in the 0.1–10 GHz range (Kang 2015, 2016). Breaks in the spectrum are usually observed to be in the 1–2 GHz. In Stroe *et al.* (2016) especially, the breaks in the spectra of the 'Sausage' and 'Toothbrush' radio relics are in the range 2–2.5 GHz. In the case of the observations presented in this paper, the break occurs close to 5 GHz. It is worth pointing out that the possibility of the break in the spectrum of the Bullet cluster occuring in the range 4.8–8.8 GHz has been pointed out (Siemieniec-Ozieblo 2004), based on DSA modeling of the radio relic.

The change/steepening in the spectral index in DSA models with radiative cooling is ~ 0.5 (e.g. Ensslin *et al.* (1998)), whereas the change we measure for our observations are ≥ 1. In Stroe *et al.* (2016), the change in the spectral index is ~ 0.5 for the 'Toothbrush' relic, and ~ 0.8 for the 'Sausage' relic. Therefore, it is safe to say that there may be variations in the spectral index change due to steepening.

Fujita *et al.* (2015) point out that the turbulent reacceleration of cosmic ray (CR) electrons behind the shock can explain the spectral steepening – which cannot be explained by the standard DSA model – in a few cluster mergers, including the Bullet cluster. Interestingly, they point out possible obscurations of relics by turbulent reacceleration-formed radio halos; while no obscuring is observed in our observations or Shimwell *et al.* (2014), both these observations detect a diffuse emission 'bridge' between the relic and the halo, which may be due to the reacceleration of the CR electrons behind the shock.

In order to explain the structure of radio relic spectra, Kang and Ryu (2015) explored DSA models where a spherical shock impinges on a population of relativistic electrons, as shown in their

Fig. 1, which details a shock front meeting an elongated structure of fossil relativistic electrons. On comparison with 'Sausage' cluster data from Stroe *et al.* (2016), they were able to explain the break in the spectrum, but not the complete shape of the spectrum. Interestingly, Shimwell *et al.* (2015) have pointed out the possibility of fossil relativistic electrons leftover from a radio galaxy causing the bright relic A, so that the modeling done by Kang and Ryu (2015) is directly applicable.

In this context, Kang and Ryu (2016) have considered the model of radio relic formation that is perhaps most relevant for the radio relic in the Bullet cluster, wherein the merger shock goes through a small-size collection of fossil electrons – this causes the spectrum to be steeper than it would be only through radiative aging. Using their simulations, Kang and Ryu (2016) were abe to reproduce the spectral curvature in the Sausage cluster as measured in Stroe *et al.* (2016). Figs. 5 & 6 in Kang and Ryu (2016) show their models, with data points from Stroe *et al.* (2016), in good agreement with their model.

In order to compare the spectrum of the radio relic with the models detailed by Kang and Ryu (2016) and Fujita *et al.* (2015), high-resolution maps of the Bullet cluster at 5.5 and 9 GHz are needed – hence the need for deep observations at these two frequencies, using the appropriate arrays, which we are going to apply for. Also, deeper radio observations along with X-ray data near the relic regions will allow us to study radio and X-ray properties of shocks in order to understand the dynamics of this merger (Datta *et al.* 2014).

In summary, our 5.5 & 9 GHz data exhibit a steepening of the spectrum of the radio relic in the Bullet cluster. Recent theoretical models may lead to a better understanding of the origin of the radio relic in the Bullet cluster, as has been demonstarted for the 'Sausage' relic – further observations with high resolution are needed at 5.5 and 9 GHz to facilitate comparison with these models.

Acknowledgements

The Australia Telescope Compact Array is part of the Australia Telescope which is funded by the Commonwealth of Australia for operation as a National Facility managed by CSIRO. SM is greatful to Maxim Voronkov, James Urquhart and the research staff at ATCA/ATNF for guidance and help with understanding the CABB system. We thank Mark Wieringa, Ravi Subrahmanyan and D. Narasimha for useful discussions. Analysis was made possible by a generous grant for Astronomy by IIT Indore. We thank the anonymous referee for their comments.

REFERENCES

Brunetti, G. and Jones, T. W. (2014). Cosmic Rays in Galaxy Clusters and Their Nonthermal Emission. *International Journal of Modern Physics D*, **23**, 30007.

Clowe, D., Bradač, M., Gonzalez, A. H., Markevitch, M., Randall, S. W., Jones, C., and Zaritsky, D. (2006). A Direct Empirical Proof of the Existence of Dark Matter. *ApJ*, **648**, L109–L113.

Datta, A., Schenck, D. E., Burns, J. O., Skillman, S. W., and Hallman, E. J. (2014). How Much can we Learn from a Merging Cold Front Cluster? Insights from X-Ray Temperature and Radio Maps of A3667. *ApJ*, **793**, 80.

Drury, L. O. (1983). An introduction to the theory of diffusive shock acceleration of energetic particles in tenuous plasmas. *Reports on Progress in Physics*, **46**, 973–1027.

Ensslin, T. A., Biermann, P. L., Klein, U., and Kohle, S. (1998). Cluster radio relics as a tracer of shock waves of the large-scale structure formation. *A&A*, **332**, 395–409.

Feretti, L., Giovannini, G., Govoni, F., and Murgia, M. (2012). Clusters of galaxies: observational properties of the diffuse radio emission. *A&A Rev.*, **20**, 54.

Fujita, Y., Takizawa, M., Yamazaki, R., Akamatsu, H., and Ohno, H. (2015). Turbulent Cosmic-Ray Reacceleration at Radio Relics and Halos in Clusters of Galaxies. *ApJ*, **815**, 116.

Halverson, N. W., Lanting, T., Ade, P. A. R., Basu, K., Bender, A. N., Benson, B. A., Bertoldi, F., Cho, H., Chon, G., Clarke, J., Dobbs, M., Ferrusca, D., Güsten, R., Holzapfel, W. L., Kovács, A., Kennedy, J., Kermish, Z., Kneissl, R., Lee, A. T., Lueker, M., Mehl, J., Menten, K. M., Muders, D., Nord, M., Pacaud, F., Plagge, T., Reichardt, C., Richards, P. L., Schaaf, R., Schilke, P., Schuller, F., Schwan, D., Spieler, H., Tucker, C., Weiss, A., and Zahn, O. (2009). Sunyaev-Zel'Dovich Effect Observations of the Bullet Cluster (1E 0657-56) with APEX-SZ. *ApJ*, **701**, 42–51.

Kang, H. (2015). Nonthermal Radiation From Relativistic Electrons Accelerated at Spherically Expanding Shocks. *Journal of Korean Astronomical Society*, **48**, 9–20.

Kang, H. (2016). Re-acceleration model for the "Toothbrush" Radio Relic. *ArXiv e-prints*.

Kang, H. and Ryu, D. (2015). Curved radio spectra of weak cluster shocks. *The Astrophysical Journal*, **809**(2), 186.

Kang, H. and Ryu, D. (2016). Re-acceleration model for radio relics with spectral curvature. *The Astrophysical Journal*, **823**(1), 13.

Liang, H., Hunstead, R. W., Birkinshaw, M., and Andreani, P. (2000). A Powerful Radio Halo in the Hottest Known Cluster of Galaxies 1E 0657-56. *ApJ*, **544**, 686–701.

Malu, S. S. and Subrahmanyan, R. (2011). 18 GHz SZ Measurements of the Bullet Cluster. *Journal of Astrophysics and Astronomy*, **32**, 541–544.

Malu, S. S., Subrahmanyan, R., Wieringa, M., and Narasimha, D. (2010). Compact Sunyaev-Zeldovich 'hole' in the Bullet Cluster. *ArXiv e-prints*.

Owers, M. S., Nulsen, P. E. J., Couch, W. J., and Markevitch, M. (2009). A High Fidelity Sample of Cold Front Clusters from the Chandra Archive. *ApJ*, **704**, 1349–1370.

Plagge, T., Benson, B. A., Ade, P. A. R., Aird, K. A., Bleem, L. E., Carlstrom, J. E., Chang, C. L., Cho, H.-M., Crawford, T. M., Crites, A. T., de Haan, T., Dobbs, M. A., George, E. M., Hall, N. R., Halverson, N. W., Holder, G. P., Holzapfel, W. L., Hrubes, J. D., Joy, M., Keisler, R., Knox, L., Lee, A. T., Leitch, E. M., Lueker, M., Marrone, D., McMahon, J. J., Mehl, J., Meyer, S. S., Mohr, J. J., Montroy, T. E., Padin, S., Pryke, C., Reichardt, C. L., Ruhl, J. E., Schaffer, K. K., Shaw, L., Shirokoff, E., Spieler, H. G., Stalder, B., Staniszewski, Z., Stark, A. A., Vanderlinde, K., Vieira, J. D., Williamson, R., and Zahn, O. (2010). Sunyaev-Zel'dovich Cluster Profiles Measured with the South Pole Telescope. *ApJ*, **716**, 1118–1135.

Reynolds, J. E. (1994). A revised flux scale for the at compact array. Technical Report 39.3/040, ATNF Technical Document Series.

Sarazin, C. L. (1988). *X-ray emission from clusters of galaxies*.

Sault, R. (2003). ATCA flux density scale at 12mm. Technical Report 39.3/124, ATNF Technical Document Series.

Sault, R. J., Staveley-Smith, L., and Brouw, W. N. (1996). An approach to interferometric mosaicing. *A&AS*, **120**, 375–384.

Shimwell, T. W., Brown, S., Feain, I. J., Feretti, L., Gaensler, B. M., and Lage, C. (2014). Deep radio observations of the radio halo of the bullet cluster 1E 0657-55.8.

Shimwell, T. W., Markevitch, M., Brown, S., Feretti, L., Gaensler, B. M., Johnston-Hollitt, M., Lage, C., and Srinivasan, R. (2015). Another shock for the Bullet cluster, and the source of seed electrons for radio relics.

Siemieniec-Ozieblo, G. (2004). A Study of Diffusive Shock Acceleration as a Process Explaining Observations of 1 E0657-56 Galaxy Cluster. *Acta Physica Polonica B*, **35**, 2131.

Stroe, A., Rumsey, C., Harwood, J. J., van Weeren, R. J., Röttgering, H. J. A., Saunders, R. D. E., Sobral, D., Perrott, Y. C., and Schammel, M. P. (2014). The highest frequency detection of a radio relic: 16 GHz AMI observations of the 'Sausage' cluster. *MNRAS*, **441**, L41–L45.

Stroe, A., Shimwell, T., Rumsey, C., van Weeren, R., Kierdorf, M., Donnert, J., Jones, T. W., Röttgering, H. J. A., Hoeft, M., Rodríguez-Gonzálvez, C., Harwood, J. J., and Saunders, R. D. E. (2016). The widest frequency radio relic spectra: observations from 150 MHz to 30 GHz. *MNRAS*, **455**, 2402–2416.

Subrahmanyan, R., Kesteven, M. J., Ekers, R. D., Sinclair, M., and Silk, J. (2000). An Australia Telescope survey for CMB anisotropies. *MNRAS*, **315**, 808–822.

van Weeren, R. J., Röttgering, H. J. A., Brüggen, M., and Hoeft, M. (2010). Particle Acceleration on Megaparsec Scales in a Merging Galaxy Cluster. *Science*, **330**, 347.

van Weeren, R. J., Röttgering, H. J. A., Intema, H. T., Rudnick, L., Brüggen, M., Hoeft, M., and Oonk, J. B. R. (2012). The "toothbrush-relic": evidence for a coherent linear 2-Mpc scale shock wave in a massive merging galaxy cluster? *A&A*, **546**, A124.

Wilson, W. E., Ferris, R. H., Axtens, P., Brown, A., Davis, E., Hampson, G., Leach, M., Roberts, P., Saunders, S., Koribalski, B. S., Caswell, J. L., Lenc, E., Stevens, J., Voronkov, M. A., Wieringa, M. H., Brooks, K., Edwards, P. G., Ekers, R. D., Emonts, B., Hindson, L., Johnston, S., Maddison, S. T., Mahony, E. K., Malu, S. S., Massardi, M., Mao, M. Y., McConnell, D., Norris, R. P., Schnitzeler, D., Subrahmanyan, R., Urquhart, J. S., Thompson, M. A., and Wark, R. M. (2011). The Australia Telescope Compact Array Broad-band Backend: description and first results. *MNRAS*, **416**, 832–856.

This preprint was prepared with the AAS LaTeX macros v5.2.